Flux-pulse-assisted readout of a fluxonium qubit

Taryn V. Stefanski[1,2,*] and Christian Kraglund Andersen[2]

[1] *Quantum Engineering Centre for Doctoral Training, H. H. Wills Physics Laboratory and Department of Electrical and Electronic Engineering, University of Bristol, Bristol BS8 1FD, United Kingdom*

[2] *QuTech and Kavli Institute of Nanoscience, Delft University of Technology, Delft 2628 CJ, Netherlands*

(Received 10 October 2023; revised 16 February 2024; accepted 3 July 2024; published 30 July 2024)

Much attention has focused on the transmon architecture for large-scale superconducting quantum devices; however, the fluxonium qubit has emerged as a possible successor. With a shunting inductor in parallel to a Josephson junction, the fluxonium offers larger anharmonicity and stronger protection against dielectric loss, leading to higher coherence times as compared to conventional transmon qubits. The interplay between the inductive and Josephson energy potentials of the fluxonium qubit leads to a rich dispersive-shift landscape when tuning the external flux. Here, we propose to exploit the features in the dispersive shift to improve qubit readout. Specifically, we report on theoretical simulations showing improved readout times and error rates by performing the readout at a flux-bias point with large dispersive shift. We expand the scheme to include different error channels and show that with an integration time of 155 ns, flux-pulse-assisted readout offers about a 5-times improvement in the signal-to-noise ratio. Moreover, we show that the performance improvement persists in the presence of finite measurement efficiency combined with quasistatic flux noise and also when considering the increased Purcell rate at the flux-pulse-assisted readout point. We suggest a set of reasonable energy parameters for the fluxonium architecture that will allow for the implementation of our proposed flux-pulse-assisted readout scheme.

DOI: 10.1103/PhysRevApplied.22.014079

I. INTRODUCTION

Two important prerequisites for meaningful quantum information processing are the ability to apply fast accurate qubit gates and subsequently perform readout of the quantum state with high fidelity. High-fidelity single-shot measurement of superconducting qubits can be achieved through the exploitation of circuit quantum electrodynamics (cQED) [1–3]. By coupling a qubit to a far-detuned resonator, where the qubit-resonator detuning is much larger than the coupling strength and resonator line width, we reach the dispersive limit. In this regime, we can perform a quantum nondemolition (QND) measurement through probing the readout resonator with coherent microwave pulses and measuring the transmitted and reflected signals that are correlated with the qubit state [1,3,4]. This method of measurement was initially implemented with a Cooper-pair box and later in a transmon architecture, and can be further extended to other novel superconducting device architectures such as the fluxonium qubit [1,3,5]. The fluxonium qubit, initially introduced in Ref. [6], is composed of a Josephson junction shunted by a capacitive and an inductive element. The qubit can be biased via an external magnetic flux applied through the loop made up of the nonlinear Josephson junction and the inductor. Ideally, fluxonium qubits have maximal coherence and relaxation times when operated with an externally applied flux bias of $\Phi_{\text{ext}}/\Phi_0 = 0.5$ also known as the "sweet spot," where $\Phi_0 = h/(2e)$ is the magnetic flux quantum. At this point, the qubit is protected to first order against flux noise and charge noise is exponentially suppressed [6–10].

As the interest in fluxonium qubits as a promising contender for quantum computation continues to grow due to their large anharmonicity and long coherence times, it is increasingly important to optimize all aspects of the fluxonium qubit, such as minimizing the readout time while increasing the fidelity [9,11]. At the half-flux-quantum point, it is desirable to have a small dispersive shift to mitigate dephasing due to residual photons in the readout resonator [12]. However, this in turn makes fast readout challenging because longer integration times are required to differentiate the qubit states with high accuracy. To combat these opposing requirements, we propose the idea of using a rapid flux pulse to tune the qubit to a flux-bias point at which there is a large dispersive shift in

*Contact author: t.v.stefanski@tudelft.nl

order to perform the readout. Recent work with transmon qubits has demonstrated state-of-the-art measurement fidelity resulting, in part, from dynamic tuning of the qubit frequency in order to reduce the qubit-resonator detuning. This dynamical flux tuning subsequently increases the dispersive-interaction strength [13]. This effect has been experimentally shown previously with transmon architectures in Refs. [14,15] and we now aim to expand the principle to fluxonium qubits. We also show this proposal to be robust, not only to variations in energy parameters due to fabrication imperfections but also in the presence of limited measurement efficiency, quasistatic flux noise, and spontaneous emission into the resonator due to the Purcell effect. Ideally, the readout scheme should not be more sensitive to flux noise than other operations, so to put the simulations of quasistatic flux noise in context, we simulate optimized single-qubit gates in the presence of this noise as well [9,11,16,17].

In this work, we first present results of simulations performed to identify an appropriate energy-parameter regime of the fluxonium qubit as a use case for implementation of fast readout via examination of the dispersive-shift landscape. We proceed to explore how the signal-to-noise ratio (SNR) and measurement fidelity are improved as a result of using a high dispersive shift during readout. Additionally, we consider limitations imposed by imperfect measurement efficiency, flux-pulse duration, and Purcell decay. Finally, using the same energy parameters, we compare the effect of quasistatic flux noise on the error rates of both readout and single-qubit gates.

II. FLUXONIUM QUBIT

An effective lumped-element circuit diagram of a fluxonium qubit coupled to a readout resonator is depicted in Fig. 1. The Hamiltonian used to describe the fluxonium qubit is

$$\hat{H}_{\text{fluxonium}} = 4E_C\hat{n}^2 + \frac{1}{2}E_L\hat{\phi}^2 - E_J\cos(\hat{\phi} - \phi_{\text{ext}}), \quad (1)$$

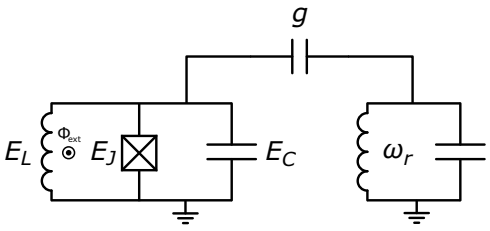

FIG. 1. The effective circuit model of a fluxonium qubit capacitively coupled to a resonator, where E_J, E_C, and E_L are the Josephson, capacitive, and inductive energies, respectively, Φ_{ext} is the flux threading the depicted loop, g is the coupling strength between the qubit and readout resonator, and ω_r is the frequency of the readout resonator.

where E_C is the charging energy of the fluxonium island, E_L is the inductive energy of the inductor, E_J is the Josephson energy, $\phi_{\text{ext}} = 2\pi(\Phi_{\text{ext}}/\Phi_0)$, and Φ_{ext} is the physical flux threading the loop shared by the Josephson junction and the inductor. It is convenient to simulate the fluxonium Hamiltonian in the harmonic oscillator basis, where the charge operator is defined as $\hat{n} = (-i/(\sqrt{2}\phi_0))(\hat{c} - \hat{c}^\dagger)$ and the flux operator takes the form $\hat{\phi} = (\phi_0/\sqrt{2})(\hat{c} + \hat{c}^\dagger)$, where $\phi_0 = (8E_C/E_L)^{1/4}$, and $\hat{c}$ and $\hat{c}^\dagger$ are the annihilation and creation operators, respectively, of the qubit basis states [18].

The resonator and coupling between the resonator and qubit, where the coupling term assumes the rotating-wave approximation, are modeled by

$$\hat{H}_{\text{resonator}} = \hbar\omega_r\left(\hat{a}^\dagger\hat{a} + \frac{1}{2}\right), \quad (2)$$

$$\hat{H}_{\text{coupling}} = \hbar g(\hat{a}\hat{c}^\dagger + \hat{a}^\dagger\hat{c}). \quad (3)$$

In these equations, $\omega_r = 1/\sqrt{LC}$ is the resonant frequency of the resonator, g is the coupling strength mediated by the coupling capacitor, and $\hat{a}^\dagger$ and $\hat{a}$ are the creation and annihilation operators of the resonator. Summing the three terms expressed in Eqs. (1)–(3) yields the total system Hamiltonian used in subsequent sections to obtain the numerical results.

III. DISPERSIVE-SHIFT LANDSCAPE

It is possible to simplify the total Hamiltonian by assuming that the fluxonium qubit acts as a two-level system and thus to use the Jaynes-Cummings model under the rotating-wave approximation to describe the system in Fig. 1. Operating in the dispersive regime, where the detuning between the qubit and resonator is much larger than the coupling strength ($|\Delta| = |\omega_r - \omega_q| \gg g$), the Hamiltonian can be expanded to second order in g/Δ using perturbation theory [19]:

$$\hat{H}_{\text{JC}} = \hbar\left(\omega_r + \frac{g^2}{\Delta}\hat{\sigma}_z\right)\hat{a}^\dagger\hat{a} + \frac{\hbar}{2}\left(\omega_q + \frac{g^2}{\Delta}\right)\hat{\sigma}_z. \quad (4)$$

In this equation, ω_q represents the qubit frequency and $\hat{\sigma}_z$ is the Pauli-Z operator.

From the first term in Eq. (4), it becomes evident that the resonator frequency is dependent on the state of the qubit. The dispersive shift refers to the amount by which the qubit state dresses the bare-resonator frequency and is denoted by $\chi = g^2/\Delta$. However, this approximate Hamiltonian neglects levels outside of the computational subspace, which play an important role in the qubit-resonator interaction for fluxonium qubits [18]. Therefore, we instead numerically diagonalize the Hamiltonian for the qubit-resonator coupled system obtained from summing Eqs. (1)–(3) in the harmonic oscillator basis and

calculate the dispersive shift. We use the basis notation |qubit, resonator⟩, which identifies the energy of the dressed state closest to that of the corresponding bare state in order to obtain the dispersive shift, χ, via

$$2\chi = (\omega_{|1,1\rangle} - \omega_{|1,0\rangle}) - (\omega_{|0,1\rangle} - \omega_{|0,0\rangle}). \tag{5}$$

All of our simulations have been performed using the NumPy and QuTiP PYTHON libraries [20–22]. Calculations of relevant matrix elements, as will be discussed below, have been done with the scQubits PYTHON library [23,24].

We aim to satisfy a moderately small dispersive shift on the order of $\chi/2\pi = 0.5$–1 MHz at $\Phi_{\text{ext}}/\Phi_0 = 0.5$, as this gives a slow dephasing rate between approximately 4.5 and 16 kHz ($T_2 \approx 60$–220 μs in the limit as $T_1 \to \infty$), with a conservative choice of effective resonator temperature of 60 mK and a resonator line width of $\kappa/2\pi = 5$ MHz [12]. At an optimal readout point, we desire a large dispersive shift on the order of $\chi/2\pi = 5$–10 MHz. Sub-100 ns readout has been demonstrated with dispersive-shift values in this range for transmon qubits [25]. Another criterion to satisfy is having minimal avoided crossings in the dispersive shift between $\Phi_{\text{ext}}/\Phi_0 = 0.5$ and the chosen readout point. This requirement is to avoid coherently swapping excitations between the resonator and qubit while flux tuning to the readout point.

In Figs. 2(a) and 2(b), we numerically solve for the fluxonium-qubit transition frequency, $\omega_q = \omega_{|1,0\rangle} - \omega_{|0,0\rangle}$, and for the dispersive shift, χ, respectively. While the behavior of ω_q is rather smooth, we note many rapidly changing features in χ. Since the fluxonium qubit is not restricted by stringent selection rules away from flux biases equaling half-integer and integer flux quanta, higher-order transitions can interact with the readout resonator, giving rise to a large dispersive shift [see Figs. 2(b)–2(h)]. In Figs. 2(c)–2(h), we display the detunings between various dressed higher-order transitions and the bare-readout-resonator frequency, where the detuning is defined as

$$\Delta_{ij} = \omega_{ij} - \omega_r, \tag{6}$$

with

$$\omega_{ij} = \omega_{|i,0\rangle} - \omega_{|j,0\rangle}.$$

Reference [18] has elucidated the fact that each higher-order transition contributes to the effective dispersive shift. The dispersive shift caused by a given qubit transition $|i\rangle \leftrightarrow |j\rangle$ is proportional to $\left|\langle i|\,\hat{n}\,|j\rangle\right|^2/\Delta_{ij}$. Thus, as $\Delta_{ij} \to 0$, we expect an increase in the magnitude of the dispersive shift. At sufficiently small detunings, the interaction is no longer considered dispersive and, thus, we want to avoid these regions, as the dynamics will be dominated by a coherent swap interaction between the fluxonium and the resonator. By matching the regions of $\Delta_{ij} = 0$ in Figs. 2(c)–2(h) with regions of diverging dispersive shift, χ, in Fig. 2(b), we can identify which specific transition causes each divergence in the dispersive shift. For instance, the two dark narrow lines in Fig. 2(b) closest to the half-flux-quantum point are caused by the $|3\rangle \leftrightarrow |1\rangle$ transition being on resonance with the readout resonator.

IV. READOUT

Fluxonium qubits with frequencies around 1 GHz or lower at the sweet spot have shown consistently high T_1

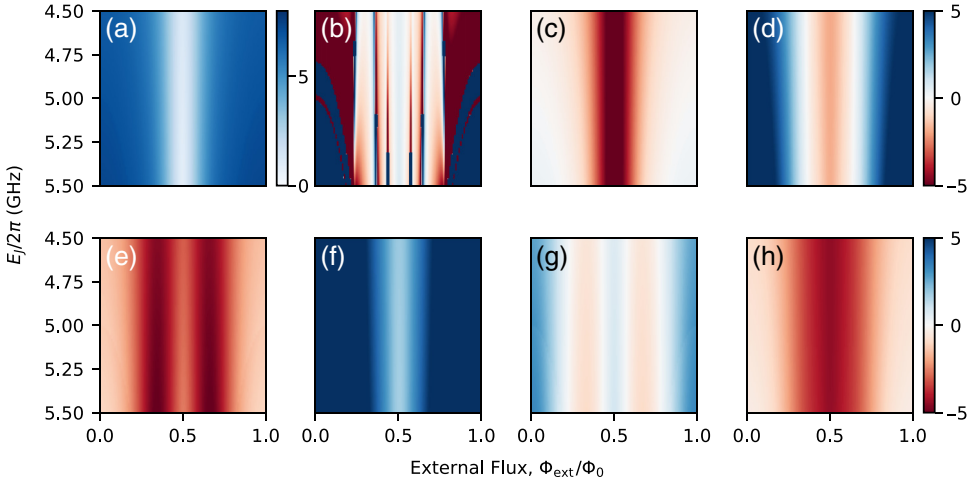

FIG. 2. The (a) qubit transition frequency, (b) dispersive shift, and (c)–(h) detuning of various fluxonium transitions from the bare-resonator frequency ($\Delta_{ij} = \omega_{ij} - \omega_r$) as a function of $E_J/2\pi$ (4.5–5.5 GHz) and the external flux, where $E_C/2\pi = 1.25$ GHz, $E_L/2\pi = 1.5$ GHz, $\omega_r/2\pi = 7$ GHz, and $g/2\pi = 50$ MHz: (a) $\omega_q/2\pi$ (GHz); (b) $\chi/2\pi$ (MHz); (c) $\Delta_{10}/2\pi$ (GHz); (d) $\Delta_{20}/2\pi$ (GHz); (e) $\Delta_{21}/2\pi$ (GHz); (f) $\Delta_{30}/2\pi$ (GHz); (g) $\Delta_{31}/2\pi$ (GHz); (h) $\Delta_{(21+10)/2}/2\pi$ (GHz). The maximum and minimum of (b) are ±5 MHz and for (c)–(h) they are ±5 GHz to provide visual clarity. Values outside of this range take on the color corresponding to the maximum or minimum value, depending on the sign. Panels (b)–(h) share the same color bar, which is depicted to the right of (d) and (h).

times exceeding 100 μs [26]. To satisfy this requirement on the qubit frequency, as well as the requirements for the dispersive shift discussed in Sec. III, we pick appropriate energy parameters for the fluxonium based on the results in Fig. 2. We propose to use a fluxonium qubit with the parameters $E_J/2\pi = 4.75$ GHz, $E_C/2\pi = 1.25$ GHz, and $E_L/2\pi = 1.5$ GHz for implementing a flux pulse during readout to improve fidelity and speed. These values have been chosen to keep both the qubit frequency and dispersive shift low at the sweet spot, as altering one of the energy parameters results in a decrease in one value but an increase in the other. Additionally, targeting these values ensures that in the case of deviations due to fabrication imperfections, the proposed readout scheme can still be implemented (see Appendix A). We note that the fluxonium qubit is symmetric about the sweet spot, so we focus our discussion on values of $\Phi_{\text{ext}}/\Phi_0 \geq 0.5$ for the rest of this section.

In order to simulate our system with the specified parameters, we use a readout-resonator frequency of $\omega_r/2\pi = 7$ GHz and a coupling strength of $g/2\pi = 50$ MHz. At the half-flux-quantum point, $\chi/2\pi \approx 0.53$ MHz and $\omega_q/2\pi \approx 1.05$ GHz. The proposed readout point is denoted with a red circle in Fig. 3 and sits at a flux bias of $\Phi_{\text{ext}}/\Phi_0 \approx 0.64$, where $\chi/2\pi \approx -8$ MHz, $\omega_q/2\pi \approx 4.6$ GHz, and $\Delta_{10}/2\pi = -2.4$ GHz. The large dispersive shift arises due to Δ_{20} approaching zero.

At the specific value we propose, we extract $\Delta_{20}/2\pi = -67$ MHz and $g_{20}/2\pi = (g/2\pi)\left|\langle 2|\,\hat{n}\,|0\rangle\right| = 18.32$ MHz. This yields a contribution to χ of $g_{20}^2/\Delta_{20} = 2\pi \times -5$ MHz and places the $|2\rangle \leftrightarrow |0\rangle$ qubit subspace on the edge of the dispersive limit. Importantly, the computational subspace of the qubit remains well into the dispersive regime at this point, with $g_{10}/2\pi = (g/2\pi)\left|\langle 1|\,\hat{n}\,|0\rangle\right| = 18$ MHz, so that $\Delta_{10} \gg g, g_{10}$. It should also be noted that while the dispersive shift more gradually approaches a large magnitude around integer multiples of flux quanta, we do not perform readout near these points, as the large values are a direct result of small detuning between the $|1\rangle \leftrightarrow |0\rangle$ qubit transition and resonator frequency.

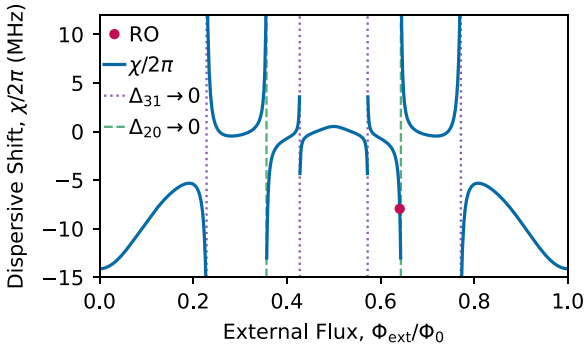

FIG. 3. The dispersive shift as a function of the external flux, where $E_J/2\pi = 4.75$ GHz, $E_C/2\pi = 1.25$ GHz, and $E_L/2\pi = 1.5$ GHz. The targeted-readout (RO) point is marked with a red circle, the blue curve shows $\chi/2\pi$, and the dashed and dotted vertical asymptotes denote where a certain qubit transition, $|i\rangle \leftrightarrow |j\rangle$, and the resonator are on resonance, denoted by $\Delta_{ij} \to 0$ in the legend.

From Fig. 3, it is evident that we must traverse a point at which the $|3\rangle \leftrightarrow |1\rangle$ qubit transition is resonant with the resonator around $\Phi_{\text{ext}}/\Phi_0 \approx 0.575$. We numerically calculate $g_{31}/2\pi = 5.81$ MHz from the size of the anticrossing, which yields a swap time of roughly 43 ns. From the Jaynes-Cummings model, the swap time is defined as $\pi/2g_{ij}$ and is the time it takes for an excitation to be exchanged between the qubit subspace and resonator, given that they are on resonance. The swap time sets an upper limit on the ramp time of the flux pulse. However, there is a trade-off between decreasing the ramp time to ensure that the QNDness of the readout is maximized (see Appendix B) and having a long enough ramp time for the process to remain adiabatic. To be considered adiabatic, the ramp time must be on a time scale $\gg 2\pi/\omega_q \approx 1$ ns [27].

In order to achieve high measurement fidelity, we aim to perform a strong measurement in a short amount of time so that we avoid relaxation of the qubit of interest. We can quantify the strength of the measurement using the SNR as a metric. This value is the ratio between the separation of the mean of the $|0\rangle$ and $|1\rangle$ state projections in the I-Q plane and the total standard deviation of the two signal distributions, which typically take on a Gaussian profile [28,29]. The separation between the distributions grows linearly in time t, compared to the width of the distributions, which scales as $\sqrt{t}$ [28]. We are in the strong-measurement regime when the SNR is greater than unity and, thereby, the two states can be distinguished because the distributions have separated after a certain amount of integration time.

We can use the Langevin equation in the context of input-output formalism in order to numerically simulate the output field of a resonator when probed with a coherent input field via a capacitively coupled drive line. This is expressed as

$$\dot{\hat{a}} = -i\chi\hat{\sigma}_z\hat{a} - \frac{1}{2}\kappa\hat{a} - \sqrt{\kappa}\hat{a}_{\text{in}}, \tag{7}$$

$$\hat{a}_{\text{out}} = \hat{a}_{\text{in}} + \sqrt{\kappa}\hat{a}, \tag{8}$$

where Eq. (8) is the boundary condition for Eq. (7), $\hat{a}_{\text{in}}$ is the coherent input field such that $\langle\hat{a}_{\text{in}}\rangle = -\epsilon/\sqrt{\kappa}$, $\hat{a}$ is the intracavity field, $\hat{a}_{\text{out}}$ is the output field, and κ is the photon decay rate into the drive line or the line width of the resonator [30–32]. Assuming that the resonator is in a coherent state as we probe it with a classical signal, Eq. (7) can alternatively be solved in terms of the coherent state

amplitude, α, from

$$\dot{\alpha} = -i\chi \left\langle \hat{\sigma}_z \right\rangle \alpha - \frac{1}{2}\kappa\alpha - \sqrt{\kappa}\alpha_{\text{in}}, \tag{9}$$

where $\alpha_{(\text{in/out})} = \left\langle \hat{a}_{(\text{in/out})} \right\rangle$. Equation (9) has the solutions

$$\alpha_{\pm} = \frac{\epsilon}{\kappa}\left[1 + e^{-i\phi_{qb}\langle\hat{\sigma}_z\rangle} \times \left(1 - 2\cos\left(\frac{\phi_{qb}}{2}\right) e^{\left(-i\chi t\langle\hat{\sigma}_z\rangle - \frac{\kappa t}{2} + i\frac{\phi_{qb}}{2}\langle\hat{\sigma}_z\rangle\right)}\right)\right]. \tag{10}$$

From Eq. (10), α_+ (α_-) is obtained when $\left\langle \hat{\sigma}_z \right\rangle$ = +1 (-1), corresponding to the qubit eigenstate $|0\rangle$ ($|1\rangle$). Additionally, t is the integration time, ϵ is the driving amplitude of the input field, and ϕ_{qb} is the phase shift of the output field caused by the qubit, defined as

$$\phi_{qb} = 2\arctan\left(\frac{2\chi}{\kappa}\right). \tag{11}$$

We can choose ϵ based on the targeted mean photon number by solving for $\overline{n}$ in the steady state in terms of the drive amplitude

$$\epsilon = \sqrt{\overline{n}\left(\frac{\kappa^2}{4} + \chi^2\right)}. \tag{12}$$

Once we have found $\alpha_{\pm}$, we can find α_{out} via the equation

$$\alpha_{\text{out}} = \alpha_{\text{in}} + \sqrt{\kappa}\alpha. \tag{13}$$

We can describe the SNR in terms of the measurement operator $\hat{M}$

$$\hat{M}(\tau) = \sqrt{\kappa\eta}\int_0^{\tau} \hat{a}_{\text{out}}(t)dt, \tag{14}$$

where we assume heterodyne detection and use η to represent the measurement efficiency. We denote $\left\langle \hat{M} \right\rangle$ as M_S and the noise operator as $\hat{M}_N = \hat{M} - \left\langle \hat{M} \right\rangle$, following the convention in Ref. [32]. The equation describing the SNR then reads as

$$\text{SNR} = \frac{|M_{S,\eta,|0\rangle} - M_{S,\eta,|1\rangle}|}{\left[\left\langle \hat{M}^2_{N,|0\rangle} \right\rangle + \left\langle \hat{M}^2_{N,|1\rangle} \right\rangle\right]^{1/2}}. \tag{15}$$

We can evaluate $\left\langle \hat{M}^2_N \right\rangle$ to $\kappa\tau/2$, where τ is the total integration time, since we are using a coherent input field.

Combining these formulas, we first calculate the SNR for conventional fluxonium readout where $\Phi_{\text{ext}}/\Phi_0 = 0.5$ and remains static (see the red lines in Fig. 4). At the half-flux-quantum point, the dispersive shift is $\chi/2\pi = 0.527$ MHz and with a resonator line width of $\kappa/2\pi = 5$ MHz, perfect measurement efficiency, and $\bar{n} = 10$, we obtain an SNR of 1 after about 155 ns.

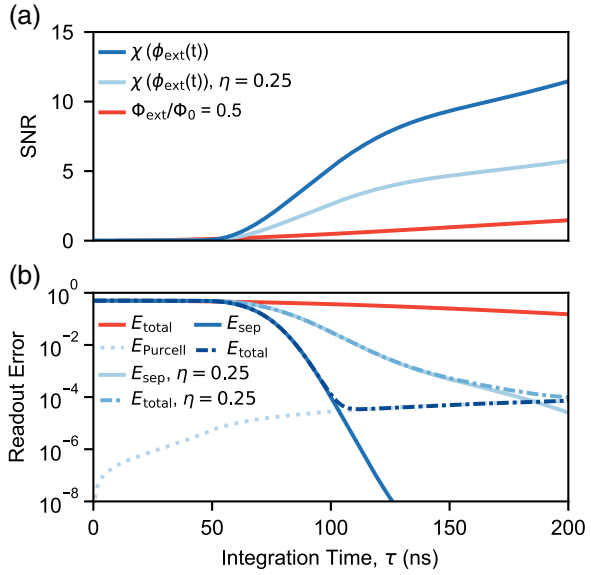

FIG. 4. A comparison of the readout at the half-flux-quantum point, where $\Phi_{\text{ext}}/\Phi_0 = 0.5$ and $\chi/2\pi = 0.527$ MHz (red), versus readout incorporating a flux pulse with a 50-ns rise time to $\Phi_{\text{ext}}/\Phi_0 = 0.641$ with $\chi/2\pi = -7.95$ MHz for measurement efficiencies of 25% (light blue, solid) and 100% (dark blue, solid). (a) The SNR versus the integration time. (b) The readout error as a function of the integration time. The solid curves show the readout error limited only by the SNR (E_{sep}). The dotted light-blue line marks the error arising from Purcell decay in the flux-pulse-assisted readout case (E_{Purcell}). The dash-dotted lines show the total error rates (E_{total}) from summing the two contributions for $\eta = 25\%$ (light) and $\eta = 100\%$ (dark).

Following our proposal, we next discern the effect of performing readout during flux tuning of the qubit. We assume a flux-pulse rise time of 50 ns and assume that the flux pulse remains on for the remaining duration of the readout. We numerically solve the Langevin equation using an explicit time-dependent dispersive shift $\chi(\phi_{\text{ext}}, t) = \chi(\phi_{\text{ext}}(t))$, following the behavior shown in Fig. 3 and assuming that the flux increases linearly from $\Phi_{\text{ext}}/\Phi_0 = 0.5$ to the target flux of $\Phi_{\text{ext}}/\Phi_0 = 0.641$ during the first 50 ns of the readout. During this time, we also quadratically increase the resonator drive amplitude, ϵ, until we reach the value given by Eq. (12). Because we are reading out at a frequency equal to the bare-resonator frequency, the gradual rise of the drive amplitude avoids populating the readout resonator at the start of the readout, where the dispersive shift is low.

The SNR slowly increases during the ramp time of the flux pulse and then increases more rapidly once the steady value of $\Phi_{\text{ext}}/\Phi_0 = 0.641$ is reached [see the blue lines

in Fig. 4(a)]. Assuming 100% measurement efficiency, the SNR is around 9.5 after 155 ns, giving almost an order-of-magnitude improvement in the SNR as compared to static readout at the sweet spot. With a realistic experimental measurement efficiency of 25%, after 155 ns the SNR is still about 5 times larger than the SNR obtained with perfect measurement efficiency when readout is performed at the sweet spot. Thus, we can more rapidly distinguish the two qubit states with high certainty via the exploitation of a strong dispersive shift. We use a long flux-pulse rise time in these simulations to numerically demonstrate proof of principle and show that we still see a substantial improvement in measurement time; potential additional speed-up could be achieved with flux-pulse parameter optimization [33,34].

From the SNR, we can also extract the SNR-limited, or separation, error from

$$E_{\text{sep}} = \frac{1}{2}\text{erfc}\left(\frac{\text{SNR}}{2}\right), \tag{16}$$

with

$$\text{erfc}(x) = 1 - \frac{2}{\sqrt{\pi}}\int_0^x e^{-t^2}dt,$$

which is modeled by the solid curves in Fig. 4(b).

As expected, the readout error trends toward zero for large times, although much more rapidly for the case in which we flux tune to the suggested readout point. Using the proposed flux-pulsing scheme, an error of 10^{-3} is reached in roughly 140 ns for the case of 25% measurement efficiency, compared to 570 ns if readout is performed at the half-flux-quantum point with perfect measurement efficiency.

We also consider the limitation imposed by an increased Purcell decay rate at the readout point compared to that at sweet spot. In the dispersive-interaction picture, the Purcell rate of decay is modeled by [35,36]

$$\Gamma_{\text{P}} = \left(\frac{g}{\Delta}\right)^2 \kappa. \tag{17}$$

We focus our attention on the computational subspace of the qubit and thus use g_{10} and Δ_{10} in evaluating Eq. (17). In this context, Δ_{10} is the difference between the bare-qubit and bare-resonator frequencies. Because Purcell decay only leads to an incorrect measurement of the ground state if the decay occurs at a time $<\tau/2$, the contribution to the readout error can be expressed as [36,37]

$$E_{\text{Purcell}} = \frac{1}{4}\left(1 - e^{-\int_0^\tau \Gamma_{\text{P}}(t)dt}\right). \tag{18}$$

At the sweet spot, we find a Purcell decay time of $T_{1,\text{P}} \approx 11$ ms, which means that the achievable readout error only becomes Purcell limited for integration times $\gtrsim$800 ns. At the flux-pulse-assisted readout point, the qubit-resonator detuning is reduced, yielding a decreased Purcell decay time of $T_{1,\text{P}} \approx 560$ μs. Flux-pulse-assisted readout becomes Purcell limited for integration times beyond about 150 ns (100 ns) with $\eta = 25\%$ (100%). Despite the increased Purcell decay rate, flux-pulse-assisted readout outperforms readout at the sweet spot for integration times up to about 650 ns and offers an advantage of at least 2 orders of magnitude for times between approximately 150 and 400 ns. One could consider employing a Purcell filter within the circuit design if further suppression of Purcell decay is desired [36,38,39].

In this section, we focus our analysis on prominent error channels that are intrinsic to the readout design and parameters. It is important to note that in practice we will also be limited by the finite relaxation time of the qubit (see Appendix C) and potential measurement-induced state transitions, which have not been accounted for in these simulations. The occurrence of measurement-induced state transitions is expected to degrade the QNDness of the readout and limit the measurement fidelity. However, simulating the precise nature and conditions of these transitions, as has been done extensively in the context of transmon qubits, goes beyond the scope of this present work [14,40–43]. Finally, due to the low frequency of the fluxonium at sweet spot, which leads to a large thermal population, any characterization of readout would be limited by the initialization fidelity. Various methods of initialization have been employed experimentally in fluxoniums with high fidelity [11,16,44–47]. Here, we assume that the qubit is perfectly initialized.

V. QUASISTATIC FLUX NOISE

Although the fluxonium qubit benefits from long coherence times partially afforded by the first-order insensitivity to flux noise at the sweet spot, our proposed protocol requires flux pulsing to a bias point that has an increased susceptibility to flux noise. The prevalent quasistatic $1/f$ noise, varying from one pulse sequence to the next, results in qubit dephasing [48]. While additional dephasing during readout is irrelevant as a strong measurement inherently dephases the qubit, we need to verify that the flux-pulse-assisted measurement performance is not limited by potential flux noise.

In this section, we simulate the presence of quasistatic flux noise by adding a constant flux-bias offset of δ during flux-pulse-assisted readout, assuming 25% measurement efficiency. We average over 50 iterations of δ for three different scaling factors. In this context, $\delta = \xi x \Phi_0$, where ξ is a scaling factor of $10^{-2}, 10^{-3}$, or 10^{-4} and x is a random number sampled from a Gaussian distribution with a mean of $\mu = 0$ and a variance of $\sigma^2 = 1$, for each iteration. The literature commonly reports flux-noise amplitudes on the order of 1–10 $\mu\Phi_0$ observed in superconducting qubit

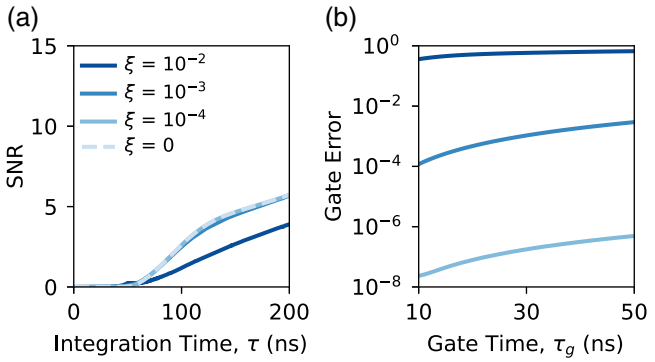

FIG. 5. A comparison of (a) the readout SNR obtained using flux-pulse-assisted readout with a measurement efficiency of 25% and (b) the single-qubit gate fidelity of a Pauli-X gate with varying amounts of quasistatic flux noise added in the form of a constant offset, δ, where $\delta = \xi x \Phi_0$ and x is a value sampled randomly from a normal Gaussian distribution.

devices [49–52]. Thus, the amount of noise that we add to our numerical simulations reflects flux noise significantly larger than that observed in state-of-the-art experiments. As displayed in Fig. 5(a), for the extreme case of $\xi = 10^{-2}$, our SNR after 155 ns is still almost 3 times larger than the SNR achieved with a static readout at the sweet spot with perfect measurement efficiency [see the red line of Fig. 4(a)]. This corresponds to a readout error of roughly 8%. In the cases of $\xi = 10^{-3}$ or 10^{-4}, there is no substantial deviation from the readout achievable in the presence of zero quasistatic flux noise. It should be noted that the small peak around 50 ns for $\xi = 10^{-2}$ is an artifact of averaging over iterations where the flux pulse overshoots the targeted-readout (RO) point such that it is closer to the $|2\rangle \leftrightarrow |0\rangle$ avoided crossing, yielding an extremely large dispersive-shift magnitude. The quasistatic flux-noise offset does not improve the readout SNR for short integration times, generally.

To put these numbers into context, we also simulate the single-qubit gate fidelity of a Pauli-X gate with a derivative removal by adiabatic gate (DRAG) pulse performed at the sweet spot in the presence of varying degrees of quasistatic flux noise in order to further characterize the achievable quality of qubit operations in the presence of this decoherence channel. Thus, our simulations serve to verify that our flux-pulse-assisted readout scheme is not the limiting factor for overall qubit performance. We add the flux-noise offset in the same manner as has been done for the readout simulations previously discussed. Prior to adding the noise, we first optimize the performance of the X_π rotation.

In order to model these single-qubit gates, we add a drive term to the Hamiltonian of the fluxonium-resonator coupled system [Eqs. (1)–(3)]. We assume that the qubit is capacitively coupled to a microwave drive line that receives signals from room-temperature electronics, the experimental parameters of which, including the pulse shape, amplitude, duration, frequency, and phase, can be altered.

The envelope function used to describe the shape of the in-phase pulse component is

$$s(t) = \frac{1}{2}\left(1 - \cos\left(\frac{2\pi t}{\tau_g}\right)\right). \tag{19}$$

We opt for a sinusoidal envelope function as in Ref. [9] in order to avoid the truncation that is necessary with a traditional Gaussian envelope function and to reduce the bandwidth of the pulse. A DRAG pulse is also applied in the out-of-phase component to help correct for leakage and pulse errors, as has been done before in transmon qubits and has been theoretically explored in scalable fluxonium architectures [9,29,53,54]. The envelope function of this pulse takes the form

$$s'(t) = \frac{\lambda}{\alpha}\frac{\partial s(t)}{\partial t}, \tag{20}$$

where λ is a scaling parameter and α is the anharmonicity of the qubit.

With this pulse shape defined, we can write the drive term of the Hamiltonian as

$$\hat{H}_{\text{drive}} = \varepsilon_d \hat{n}[2s(t)\sin(\omega_d t) + s'(t)\cos(\omega_d t)], \tag{21}$$

where ε_d is the drive amplitude and ω_d is the frequency of the drive signal.

We first optimize over ε_d and λ, assuming that $\omega_d = \omega_{q,\varphi_{\text{ext}}=\pi}$, for gate times ranging from 10 to 50 ns. We subsequently add the flux-noise offset to the single-qubit-gate performance with optimized parameters. These results are presented in Fig. 5(b). In the noisiest case simulated with $\xi = 10^{-2}$, our single-qubit-gate error has a high value of 36% with a gate time of 10 ns, which is an order of magnitude worse than the readout error induced by this level of flux noise. If we compare the single-qubit-gate error curves in the cases of $\xi = 10^{-3}$ and 10^{-4}, we see that a one-order-of-magnitude increase in quasistatic flux noise degrades the gate error by 4 orders of magnitude. Thus, we observe that our flux-pulse-assisted readout scheme is more robust than optimized single-qubit gates in the face of quasistatic $1/f$ flux noise.

VI. CONCLUSIONS AND OUTLOOK

In summary, we present a proposal for performing fast flux-pulse-assisted high-fidelity readout of a fluxonium qubit with one set of optimized energy parameters. We suggest appropriate values of Josephson, capacitive, and inductive energies for a fluxonium qubit, which will enable our readout proposal based on the simulated dispersive-shift landscape. Future work may consider exploring the

TABLE I. A summary of the readout errors for readout at the sweet spot compared to the flux-pulse-assisted readout scheme after an integration time of 200 ns. The bottom row quantifies the level of non-QNDness expected to arise from traversing the $|3\rangle \rightarrow |1\rangle$ avoided crossing during the flux-pulse ramp.

Error	Sweet spot	Flux-pulse-assisted
Purcell decay	4.5×10^{-6}	7.2×10^{-5}
Dielectric loss	2.4×10^{-4}	5.7×10^{-4}
Thermal excitation	1.9×10^{-5}	9.3×10^{-7}
Signal separation	0.15	2.7×10^{-16}
	25-ns flux ramp	50-ns flux ramp
Non-QNDness	6.5×10^{-4}	4.8×10^{-3}

implementation of this scheme in more novel energy regimes, such as the heavy-fluxonium regime [47,55].

We demonstrate the improvement in measurement speed and fidelity that can be obtained by exploiting a large dispersive shift when the qubit is detuned from the sweet spot, despite an increased Purcell decay rate and susceptibility to flux noise at this point. In this work, we do not explicitly consider swap dynamics or changes in the dispersive shift due to ac Stark shifting during measurement, however, we expect that this can be compensated for through flux-pulse calibration. Pulse-shaping techniques may also be utilized to further reduce the time required for the scheme. We present the readout SNR and single-qubit-gate fidelity achievable in the presence of varying degrees of quasistatic flux noise. Finally, we compare the contribution of various error channels discussed in the text in the context of both readout at the sweet spot and with flux-pulse-assisted readout. These quantities are listed in Table I, with the addition of error resulting from thermal excitation. Our simulated results show a robust improvement in both the readout speed and the fidelity when the proposed protocol is implemented.

The code used to generate these numerical results is available in Ref. [56].

ACKNOWLEDGMENTS

We thank J. Heinsoo and M.F.S. Zwanenburg for insightful discussions. T.V.S. acknowledges the support of the Engineering and Physical Sciences Research Council (EPSRC) under Grant No. EP/SO23607/1. C.K.A. additionally acknowledges support from the Dutch Research Council (NWO).

APPENDIX A: FABRICATION VARIATIONS

The translation of the theoretical energy parameters to those of a working device may prove challenging in practice. Careful calibration required of fabrication processes, material defects, and device aging may lead to deviations

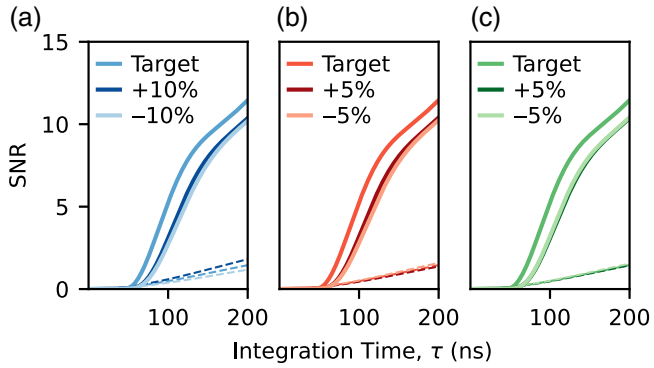

FIG. 6. The SNR versus the integration time for variations in the qubit energy parameters from the targeted values of (a) E_J, (b) E_L, and (c) E_C. In changing one energy parameter, the other two are maintained at the targeted values. The solid lines denote the resulting SNR achieved with flux-pulse-assisted readout, utilizing a readout point with parameters (see Table II) that are comparable to those used in the main text. The dashed lines show the SNR achieved using static readout at the sweet spot.

of qubit parameters from targeted values [57]. In order to look at the robustness of our proposal, we compare the SNR attainable during flux-pulse-assisted readout when one of the fluxonium energy parameters is varied from the value proposed in the main text. We consider an error of $\pm 5\%$ in the case of E_L and E_C and an error of $\pm 10\%$ in the case of E_J. We account for greater variation in the Josephson energy as it is more prone to deviations because of the small size of the single-junction area that must be precisely targeted [58–60]. In Fig. 6, we compare the achievable SNR using static, sweet-spot (dashed lines) and flux-pulse-assisted (solid lines) readout when each fluxonium energy parameter is independently subjected to a small perturbation.

In each instance, we exploit the dispersive-shift feature arising from $\Delta_{20} \rightarrow 0$ and ensure that the computational subspace is well into the dispersive regime. The exact parameter values are listed in Table II. The amplitude of the flux pulse is adjusted in each case to achieve comparable dispersive shift, effective coupling, and detuning values at the readout point, and the drive amplitude is updated accordingly. The other relevant readout parameters, including the resonator frequency, resonator line width, and total coupling, are kept constant.

Although both positive and negative fluctuations in all three fluxonium energy parameters cause slight degradation in the SNR compared to when we have perfect targeting, it is evident that we retain the advantage provided by flux-pulse-assisted readout. The case of $E_J/2\pi = 4.275$ GHz yields the largest drop in the SNR and yet still reaches an SNR of about 8 after only a 155-ns integration time. This value is a substantial improvement compared to the SNR achieved with static readout at the sweet spot.

TABLE II. An overview of the fluxonium energy and readout parameters used to simulate the performance of flux-pulse-assisted readout with variations from the targeted values of $E_J/2\pi = 4.75$ GHz, $E_L/2\pi = 1.5$ GHz, and $E_C/2\pi = 1.25$ GHz that may result from fabrication. The subscripts SS and RO denote values at the sweet spot and readout point, respectively.

Energy variations	$E_J/2\pi$ (GHz)	$E_L/2\pi$ (GHz)	$E_C/2\pi$ (GHz)	$\omega_{q,\mathrm{SS}}/2\pi$ (GHz)	$\chi_{\mathrm{SS}}/2\pi$ (MHz)	$\Phi_{\mathrm{ext,RO}}/\Phi_0$ (arb. units)	$\omega_{q,\mathrm{RO}}/2\pi$ (GHz)	$\chi_{\mathrm{RO}}/2\pi$ (MHz)	$g_{20,\mathrm{RO}}/2\pi$ (MHz)	$\Delta_{20,\mathrm{RO}}/2\pi$ (MHz)
$E_J/2\pi + 10\%$	5.225	1.5	1.25	0.871	0.649	0.635	4.74	−7.69	20.2	−85.1
$E_J/2\pi - 10\%$	4.275	1.5	1.25	1.25	0.425	0.645	4.42	−7.00	16.6	−62.3
$E_L/2\pi + 5\%$	4.75	1.575	1.25	1.12	0.493	0.633	4.49	−7.86	18.2	−66.4
$E_L/2\pi - 5\%$	4.75	1.425	1.25	0.974	0.570	0.649	4.72	−7.15	18.4	−76.6
$E_C/2\pi + 5\%$	4.75	1.5	1.3125	1.12	0.519	0.632	4.41	−7.65	18.6	−74.2
$E_C/2\pi - 5\%$	4.75	1.5	1.1875	0.975	0.555	0.649	4.77	−7.93	17.8	−61.3

APPENDIX B: COHERENT EXCHANGE DURING FLUX-PULSE RAMPING

Our flux-pulse-assisted readout scheme with the proposed parameters requires traversing the avoided crossing of the $|3\rangle \leftrightarrow |1\rangle$ qubit transition and readout resonator. We quantify the non-QNDness resulting from the exchange interaction during the 50-ns flux-pulse ramp time. We consider the two-dimensional Hilbert space spanned by $|1,1\rangle$ and $|3,0\rangle$. We then construct the time-dependent Jaynes-Cummings Hamiltonian within this subspace:

$$\hat{H}_{\mathrm{JC},31}(t) = \frac{\hbar\Delta_{31}(t)}{2}\hat{\sigma}_z + \hbar\,|\alpha_-(t)|\,g_{31}(t)\hat{\sigma}_x. \tag{B1}$$

In this Hamiltonian, Δ_{31} is the difference between the bare-qubit $|3\rangle \leftrightarrow |1\rangle$ transition and bare-resonator frequencies and α_- is the intracavity resonator field as in Eq. (10). The time dependence arises as the parameters change while the external flux bias is being linearly ramped from $\Phi_{\mathrm{ext}}/\Phi_0 = 0.5$ to 0.641. Assuming that $|1,1\rangle$ is our initial state, we solve for the population of $|3,0\rangle$ at the end of the flux ramping via a time evolution generated by Eq. (B1) (see Fig. 7). We refer to the amount of exchanged state population as the non-QNDness.

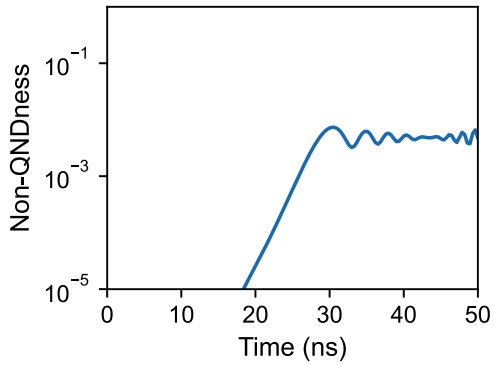

FIG. 7. The non-QNDness as a function of time for 50-ns linear ramping of the flux pulse used to tune the qubit. This figure considers the population transferred from the resonator to the third qubit excited state as the avoided crossing around $\Phi_{\mathrm{ext}}/\Phi_0 \approx 0.575$ is traversed.

For a 50-ns rise time, our non-QNDness oscillates around 4.8×10^{-3} once the $|3\rangle \rightarrow |1\rangle$ avoided crossing has been passed. It is possible to reduce this by shortening the rise time to 25 ns, yielding a non-QNDness that oscillates about 6.5×10^{-4} post avoided crossing. However, in doing so, we trade off with the adiabaticity of the flux ramping. Finally, pulse shaping of the flux pulse to rapidly cross the avoided crossing may further reduce the non-QNDness.

APPENDIX C: EFFECT OF RELAXATION TIME ON READOUT ERROR

In the main text, we discuss limitations of the flux-pulse-assisted readout scheme that are intrinsic to the readout design. However, relaxation of the qubit inevitably limits the fidelity of fundamental operations, irrespective of the readout method. Dielectric loss, which is dictated by the structure geometry and material properties, largely limits the qubit relaxation times [61]. For frequencies above approximately 1 GHz, we can use the dielectric loss model with a frequency-independent loss tangent to predict the relaxation rate of the fluxonium qubit according to [17,26,62]

$$\Gamma_1 = \frac{\hbar\omega_q^2}{4E_C}\left|\langle 1|\,\hat{\phi}\,|0\rangle\right|^2 \tan\delta_C \coth\left(\frac{\hbar\omega_q}{2k_B T_{\mathrm{eff}}}\right). \tag{C1}$$

Assuming a dielectric loss tangent of $\tan\delta_C = 0.8 \times 10^{-6}$ and an effective temperature of $T_{\mathrm{eff}} = 20$ mK, we achieve $T_1 \approx 210$ μs at the sweet spot and $T_1 \approx 77$ μs at the readout point [17,26,47]. We can convert this contribution to readout error in the same manner as in Eq. (18), replacing Γ_{P} with Γ_1. After a 200-ns integration time, the error contribution to the flux-pulse-assisted readout is 5.7×10^{-4}, compared to an error of 2.4×10^{-4} during readout at the sweet spot. Further reduction in the dielectric loss tangent via attention to materials and fabrication can aid in reducing these errors.

[1] A. Blais, R.-S. Huang, A. Wallraff, S. M. Girvin, and R. J. Schoelkopf, Cavity quantum electrodynamics for superconducting electrical circuits: An architecture for quantum computation, Phys. Rev. A **69**, 062320 (2004).

[2] R. J. Schoelkopf and S. M. Girvin, Wiring up quantum systems, Nature **451**, 664 (2008).

[3] A. Wallraff, D. I. Schuster, A. Blais, L. Frunzio, R.-S. Huang, J. Majer, S. Kumar, S. M. Girvin, and R. J. Schoelkopf, Strong coupling of a single photon to a superconducting qubit using circuit quantum electrodynamics, Nature **431**, 162 (2004).

[4] V. B. Braginsky, Y. I. Vorontsov, and K. S. Thorne, Quantum nondemolition measurements, Science **209**, 547 (1980).

[5] J. Koch, T. M. Yu, J. Gambetta, A. A. Houck, D. I. Schuster, J. Majer, A. Blais, M. H. Devoret, S. M. Girvin, and R. J. Schoelkopf, Charge-insensitive qubit design derived from the Cooper pair box, Phys. Rev. A **76**, 042319 (2007).

[6] V. E. Manucharyan, J. Koch, L. I. Glazman, and M. H. Devoret, Fluxonium: Single cooper-pair circuit free of charge offsets, Science **326**, 113 (2009).

[7] A. Gyenis, A. Di Paolo, J. Koch, A. Blais, A. A. Houck, and D. I. Schuster, Moving beyond the transmon: Noise-protected superconducting quantum circuits, PRX Quantum **2**, 030101 (2021).

[8] Y.-H. Lin, L. B. Nguyen, N. Grabon, J. San Miguel, N. Pankratova, and V. E. Manucharyan, Demonstration of protection of a superconducting qubit from energy decay, Phys. Rev. Lett. **120**, 150503 (2018).

[9] L. B. Nguyen, G. Koolstra, Y. Kim, A. Morvan, T. Chistolini, S. Singh, K. N. Nesterov, C. Jünger, L. Chen, Z. Pedramrazi *et al.*, Blueprint for a high-performance fluxonium quantum processor, PRX Quantum **3**, 037001 (2022).

[10] J. Koch, V. Manucharyan, M. H. Devoret, and L. I. Glazman, Charging effects in the inductively shunted Josephson junction, Phys. Rev. Lett. **103**, 217004 (2009).

[11] F. Bao, H. Deng, D. Ding, R. Gao, X. Gao, C. Huang, X. Jiang, H.-S. Ku, Z. Li, X. Ma *et al.*, Fluxonium: An alternative qubit platform for high-fidelity operations, Phys. Rev. Lett. **129**, 010502 (2022).

[12] Z. Wang, S. Shankar, Z. K. Minev, P. Campagne-Ibarcq, A. Narla, and M. H. Devoret, Cavity attenuators for superconducting qubits, Phys. Rev. Appl. **11**, 014031 (2019).

[13] F. Swiadek, R. Shillito, P. Magnard, A. Remm, C. Hellings, N. Lacroix, Q. Ficheux, D. C. Zanuz, G. J. Norris, A. Blais *et al.*, Enhancing dispersive readout of superconducting qubits through dynamic control of the dispersive shift: Experiment and theory, arXiv:2307.07765.

[14] D. Sank, Z. Chen, M. Khezri, J. Kelly, R. Barends, B. Campbell, Y. Chen, B. Chiaro, A. Dunsworth, A. Fowler *et al.*, Measurement-induced state transitions in a superconducting qubit: Beyond the rotating wave approximation, Phys. Rev. Lett. **117**, 190503 (2016).

[15] S. Krinner, N. Lacroix, A. Remm, A. Di Paolo, E. Genois, C. Leroux, C. Hellings, S. Lazar, F. Swiadek, J. Herrmann *et al.*, Realizing repeated quantum error correction in a distance-three surface code, Nature **605**, 669 (2022).

[16] I. N. Moskalenko, I. A. Simakov, N. N. Abramov, A. A. Grigorev, D. O. Moskalev, A. A. Pishchimova, N. S. Smirnov, E. V. Zikiy, I. A. Rodionov, and I. S. Besedin, High fidelity two-qubit gates on fluxoniums using a tunable coupler, npj Quantum Inf. **8**, 1 (2022).

[17] A. Somoroff, Q. Ficheux, R. A. Mencia, H. Xiong, R. Kuzmin, and V. E. Manucharyan, Millisecond coherence in a superconducting qubit, Phys. Rev. Lett. **130**, 267001 (2023).

[18] G. Zhu, D. G. Ferguson, V. E. Manucharyan, and J. Koch, Circuit qed with fluxonium qubits: Theory of the dispersive regime, Phys. Rev. B **87**, 024510 (2013).

[19] D. I. Schuster, Ph.D. thesis, Circuit quantum electrodynamics, Yale University (2007).

[20] J. R. Johansson, P. D. Nation, and F. Nori, QuTiP: An open-source PYTHON framework for the dynamics of open quantum systems, Comput. Phys. Commun. **183**, 1760 (2012).

[21] J. R. Johansson, P. D. Nation, and F. Nori, QuTiP 2: A PYTHON framework for the dynamics of open quantum systems, Comput. Phys. Commun. **184**, 1234 (2013).

[22] C. R. Harris *et al.*, Array programming with NumPy, Nature **585**, 357 (2020).

[23] P. Groszkowski and J. Koch, scQubits: A PYTHON package for superconducting qubits, Quantum **5**, 583 (2021).

[24] S. P. Chitta, T. Zhao, Z. Huang, I. Mondragon-Shem, and J. Koch, Computer-aided quantization and numerical analysis of superconducting circuits, New J. Phys. **24**, 103020 (2022).

[25] T. Walter, P. Kurpiers, S. Gasparinetti, P. Magnard, A. Potočnik, Y. Salathé, M. Pechal, M. Mondal, M. Oppliger, C. Eichler *et al.*, Rapid high-fidelity single-shot dispersive readout of superconducting qubits, Phys. Rev. Appl. **7**, 054020 (2017).

[26] L. B. Nguyen, Y.-H. Lin, A. Somoroff, R. Mencia, N. Grabon, and V. E. Manucharyan, High-coherence fluxonium qubit, Phys. Rev. X **9**, 041041 (2019).

[27] J. J. Sakurai and J. Napolitano, *Modern Quantum Mechanics* (Cambridge University Press, Cambridge, United Kingdom, 2020), 3rd ed.

[28] A. A. Clerk, M. H. Devoret, S. M. Girvin, F. Marquardt, and R. J. Schoelkopf, Introduction to quantum noise, measurement, and amplification, Rev. Modern Phys. **82**, 1155 (2010).

[29] P. Krantz, M. Kjaergaard, F. Yan, T. P. Orlando, S. Gustavsson, and W. D. Oliver, A quantum engineer's guide to superconducting qubits, Appl. Phys. Rev. **6**, 021318 (2019).

[30] C. Gardiner and P. Zoller, *Quantum Noise: A Handbook of Markovian and Non-Markovian Quantum Stochastic Methods With Applications to Quantum Optics* (Springer Science & Business Media, Heidelberg, Germany, 2004).

[31] N. Didier, J. Bourassa, and A. Blais, Fast quantum nondemolition readout by parametric modulation of longitudinal qubit-oscillator interaction, Phys. Rev. Lett. **115**, 203601 (2015).

[32] N. Didier, A. Kamal, W. D. Oliver, A. Blais, and A. A. Clerk, Heisenberg-limited qubit read-out with two-mode squeezed light, Phys. Rev. Lett. **115**, 093604 (2015).

[33] J. Bryon, D. K. Weiss, X. You, S. Sussman, X. Croot, Z. Huang, J. Koch, and A. Houck, Time-dependent magnetic flux in devices for circuit quantum electrodynamics, Phys. Rev. Appl. **19**, 034031 (2023).

[34] Y. Chen, K. N. Nesterov, V. E. Manucharyan, and M. G. Vavilov, Fast flux entangling gate for fluxonium circuits, Phys. Rev. Appl. **18**, 034027 (2022).
[35] A. A. Houck, J. A. Schreier, B. R. Johnson, J. M. Chow, J. Koch, J. M. Gambetta, D. I. Schuster, L. Frunzio, M. H. Devoret, S. M. Girvin *et al.*, Controlling the spontaneous emission of a superconducting transmon qubit, Phys. Rev. Lett. **101**, 080502 (2008).
[36] E. A. Sete, J. M. Martinis, and A. N. Korotkov, Quantum theory of a bandpass Purcell filter for qubit readout, Phys. Rev. A **92**, 012325 (2015).
[37] M. Khezri, J. Dressel, and A. N. Korotkov, Qubit measurement error from coupling with a detuned neighbor in circuit qed, Phys. Rev. A **92**, 052306 (2015).
[38] M. D. Reed, B. R. Johnson, A. A. Houck, L. DiCarlo, J. M. Chow, D. I. Schuster, L. Frunzio, and R. J. Schoelkopf, Fast reset and suppressing spontaneous emission of a superconducting qubit, Appl. Phys. Lett. **96**, 203110 (2010).
[39] J. Heinsoo, C. K. Andersen, A. Remm, S. Krinner, T. Walter, Y. Salathé, S. Gasparinetti, J.-C. Besse, A. Potočnik, A. Wallraff *et al.*, Rapid high-fidelity multiplexed readout of superconducting qubits, Phys. Rev. Appl. **10**, 034040 (2018).
[40] M. Khezri, A. Opremcak, Z. Chen, K. C. Miao, M. McEwen, A. Bengtsson, T. White, O. Naaman, D. Sank, A. N. Korotkov *et al.*, Measurement-induced state transitions in a superconducting qubit: Within the rotating-wave approximation, Phys. Rev. Appl. **20**, 054008 (2023).
[41] R. Shillito, A. Petrescu, J. Cohen, J. Beall, M. Hauru, M. Ganahl, A. G. M. Lewis, G. Vidal, and A. Blais, Dynamics of transmon ionization, Phys. Rev. Appl. **18**, 034031 (2022).
[42] M. F. Dumas, B. Groleau-Paré, A. McDonald, M. H. Muñoz-Arias, C. Lledó, B. D'Anjou, and A. Blais, Unified picture of measurement-induced ionization in the transmon, arXiv:2402.06615.
[43] K. N. Nesterov and I. V. Pechenezhskiy, Measurement-induced state transitions in dispersive qubit readout schemes, arXiv:2402.07360.
[44] L. Ding, M. Hays, Y. Sung, B. Kannan, J. An, A. Di Paolo, A. H. Karamlou, T. M. Hazard, K. Azar, D. K. Kim *et al.*, High-fidelity frequency-flexible two-qubit fluxonium gates with a transmon coupler, Phys. Rev. X **13**, 031035 (2023).
[45] D. Gusenkova, M. Spiecker, R. Gebauer, M. Willsch, D. Willsch, F. Valenti, N. Karcher, L. Grünhaupt, I. Takmakov, P. Winkel *et al.*, Quantum nondemolition dispersive readout of a superconducting artificial atom using large photon numbers, Phys. Rev. Appl. **15**, 064030 (2021).
[46] J. E. Johnson, C. Macklin, D. H. Slichter, R. Vijay, E. B. Weingarten, J. Clarke, and I. Siddiqi, Heralded state preparation in a superconducting qubit, Phys. Rev. Lett. **109**, 050506 (2012).
[47] H. Zhang, S. Chakram, T. Roy, N. Earnest, Y. Lu, Z. Huang, D. K. Weiss, J. Koch, and D. I. Schuster, Universal fast-flux control of a coherent, low-frequency qubit, Phys. Rev. X **11**, 011010 (2021).
[48] J. Bylander, S. Gustavsson, F. Yan, F. Yoshihara, K. Harrabi, G. Fitch, D. G. Cory, Y. Nakamura, J.-S. Tsai, and W. D. Oliver, Noise spectroscopy through dynamical decoupling with a superconducting flux qubit, Nat. Phy. **7**, 565 (2011).
[49] J. Braumüller, L. Ding, A. P. Vepsäläinen, Y. Sung, M. Kjaergaard, T. Menke, R. Winik, D. Kim, B. M. Niedzielski, A. Melville *et al.*, Characterizing and optimizing qubit coherence based on squid geometry, Phys. Rev. Appl. **13**, 054079 (2020).
[50] A. Kou, W. C. Smith, U. Vool, R. T. Brierley, H. Meier, L. Frunzio, S. M. Girvin, L. I. Glazman, and M. H. Devoret, Fluxonium-based artificial molecule with a tunable magnetic moment, Phys. Rev. X **7**, 031037 (2017).
[51] S. Gustavsson, J. Bylander, F. Yan, W. D. Oliver, F. Yoshihara, and Y. Nakamura, Noise correlations in a flux qubit with tunable tunnel coupling, Phys. Rev. B **84**, 014525 (2011).
[52] F. Yoshihara, K. Harrabi, A. O. Niskanen, Y. Nakamura, and J. S. Tsai, Decoherence of flux qubits due to $1/f$ flux noise, Phys. Rev. Lett. **97**, 167001 (2006).
[53] F. Motzoi, J. M. Gambetta, P. Rebentrost, and F. K. Wilhelm, Simple pulses for elimination of leakage in weakly nonlinear qubits, Phys. Rev. Lett. **103**, 110501 (2009).
[54] J. M. Gambetta, F. Motzoi, S. T. Merkel, and F. K. Wilhelm, Analytic control methods for high-fidelity unitary operations in a weakly nonlinear oscillator, Phys. Rev. A **83**, 012308 (2011).
[55] N. Earnest, S. Chakram, Y. Lu, N. Irons, R. K. Naik, N. Leung, L. Ocola, D. A. Czaplewski, B. Baker, J. Lawrence *et al.*, Realization of a λ system with metastable states of a capacitively shunted fluxonium, Phys. Rev. Lett. **120**, 150504 (2018).
[56] https://github.com/AndersenQubitLab/FluxPulseAssistedFluxonium
[57] I. M. Pop, T. Fournier, T. Crozes, F. Lecocq, I. Matei, B. Pannetier, O. Buisson, and W. Guichard, Fabrication of stable and reproducible submicron tunnel junctions, J. Vac. Sci. Technol. B **30**, 010607 (2012).
[58] A. A. Pishchimova, N. S. Smirnov, D. A. Ezenkova, E. A. Krivko, E. V. Zikiy, D. O. Moskalev, A. I. Ivanov, N. D. Korshakov, and I. A. Rodionov, Improving Josephson junction reproducibility for superconducting quantum circuits: Junction area fluctuation, Sci. Rep. **13**, 6772 (2023).
[59] A. Osman, J. Simon, A. Bengtsson, S. Kosen, P. Krantz, D. P Lozano, M. Scigliuzzo, P. Delsing, J. Bylander, and A. Fadavi Roudsari, Simplified Josephson-junction fabrication process for reproducibly high-performance superconducting qubits, Appl. Phys. Lett. **118**, 064002 (2021).
[60] J. M. Kreikebaum, K. P. O'Brien, A. Morvan, and I. Siddiqi, Improving wafer-scale Josephson junction resistance variation in superconducting quantum coherent circuits, Supercond. Sci. Technol. **33**, 06LT02 (2020).
[61] C. Wang, C. Axline, Y. Y. Gao, T. Brecht, Y. Chu, L. Frunzio, M. Devoret, and R. J. Schoelkopf, Surface participation and dielectric loss in superconducting qubits, Appl. Phys. Lett. **107**, 162601 (2015).
[62] H. Sun, F. Wu, H. S. Ku, X. Ma, J. Qin, Z. Song, T. Wang, G. Zhang, J. Zhou, Y. Shi *et al.*, Characterization of loss mechanisms in a fluxonium qubit, Phys. Rev. Appl. **20**, 034016 (2023).